JACS Au
AN OPEN ACCESS JOURNAL OF THE AMERICAN CHEMICAL SOCIETY

pubs.acs.org/jacsau
Article

Aza[6]- and Aza[7]helicenes: Synthesis and Reversible Protonation-Induced Tuning of Photophysical and Chiroptical Properties

Felix R. Schumann, Clotilde Philippe, Pascal Weisenburger, Jeanne Crassous, and Joachim Podlech*

Cite This: https://doi.org/10.1021/jacsau.6c00315
Read Online

ABSTRACT: The development of molecular switches represents a versatile approach to the design of smart optical materials. Here, we report a protonation-induced reorientation of the transition dipole moments in a series of newly designed azahelicenes, establishing a distinctive molecular mechanism for chiroptical switching. To access these systems, we developed an efficient synthetic strategy based on intramolecular *ortho* cyclization, enabling a modular platform for carbazole- and phenanthridine-containing hexa- and heptahelicenes. The synthesized azahelicenes exhibit remarkable fluorescence properties, including quantum yields up to 30% and striking protonation-induced red-shifts of up to 151 nm (0.98 eV). Upon enantiomeric separation of representative derivatives by chiral HPLC, the azahelicenes show significant chiroptical activity with luminescence dissymmetry factors g_{lum} reaching 3.5×10^{-3}. Detailed photophysical and quantum-chemical analysis reveals that protonation of the basic nitrogen centers triggers a reversible electronic reconfiguration, modulating both emission efficiency and chiroptical response. Notably, the mechanistic origin of this switching was traced back to a protonation-induced redirection of the transition dipole moments, as confirmed by our vector-based analysis. Supported by single-crystal X-ray diffraction and quantum-chemical calculations, this work provides a basis for developing new tunable azahelicenes.

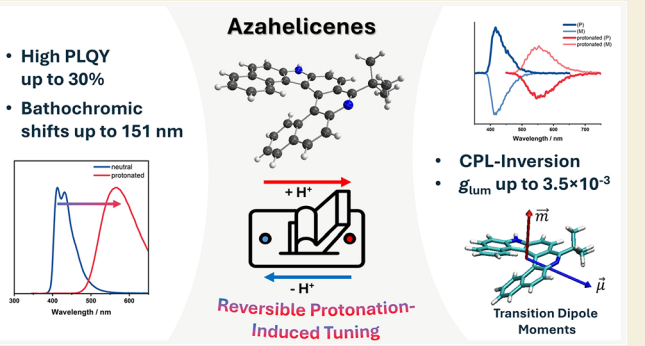

KEYWORDS: *azahelicenes, ortho fusion, molecular switching, photophysics, DFT calculations, protonation effects*

INTRODUCTION

Helicenes constitute a distinctive class of polyaromatic compounds due to their unique helical architecture arising from a consecutive *ortho* fusion of benzene rings.[1] When more than five benzene rings are fused, the resulting helical configurations are increasingly stable due to an increasing steric hindrance.[2] Their intrinsic chirality imparted by the helical framework endows these compounds with characteristic optoelectronic properties, including circular dichroism (ECD) and circularly polarized luminescence (CPL).[3] Consequently, helicenes have attracted considerable attention not only in the field of organic electronics[4] but also as asymmetric catalysts[5] and molecular sensors.[6] Like many other polyaromatic systems, helicenes exhibit fluorescence, although their quantum yields are generally modest.[7] Beyond emission, the chiroptical behavior of helicenes – quantified by the dissymmetry factor g_{lum} – is a key performance metric for next-generation photonic applications. However, achieving high luminescence dissymmetry while maintaining appreciable quantum yields remains challenging because these parameters often demand opposing structural requirements.[8]

Incorporating heteroatoms such as B, N, O, Si, P, or S allows the properties of helicenes to be tuned effectively.[9] Among these, azahelicenes are of particular relevance.[3c,d] Their synthesis is facilitated by the many possibilities for incorporating nitrogen into the molecular framework. Moreover, key properties such as electron richness or electron deficiency, redox potentials, coordination chemistry, and aromaticity can be modulated through the presence of nitrogen atoms.[9b] The basicity of the nitrogen centers in azahelicenes introduces a unique handle for external stimulation. Protonation alters the electronic structure and can induce a reorganization of the chiroptical response.[10] Such stimulation-responsive behavior with the potential for sign inversion in circular dichroism and circularly polarized luminescence positions azahelicenes as versatile candidates for molecular chiroptical switches. The concept of electron-donating (push) and -accepting (pull) groups has attracted significant attention in the design of functional organic compounds. In such systems, the highest occupied molecular orbital (HOMO) is primarily localized on the electron-donating unit, while the

Received: March 4, 2026
Revised: April 2, 2026
Accepted: April 3, 2026

lowest unoccupied molecular orbital (LUMO) is mainly associated with the electron-accepting moiety.[11] This spatial separation of frontier orbitals promotes intramolecular charge transfer (ICT) upon excitation, frequently giving rise to tunable optical properties, such as pronounced solvatochromism and large Stokes shifts.[12]

Building upon our group's expertise in constructing aza-,[13] thia-,[14] and carbohelicenes,[15] we here strategically extend these cyclization architectures to complex indolophenanthridine frameworks. Starting from *ortho*-fused terphenyl precursors **A** or **B**, the helical core **C** is assembled through a combination of tailored cyclization strategies (Scheme 1). These include the thermal cyclization of azides to form carbazoles and the *Morgan-Walls* reaction for constructing phenanthridine units; leveraging these methods allowed us to systematically build the azahelicene frameworks **D**−**F** as a platform for investigating electronic tuning.

Scheme 1. General Approach to the Target Compounds[a]

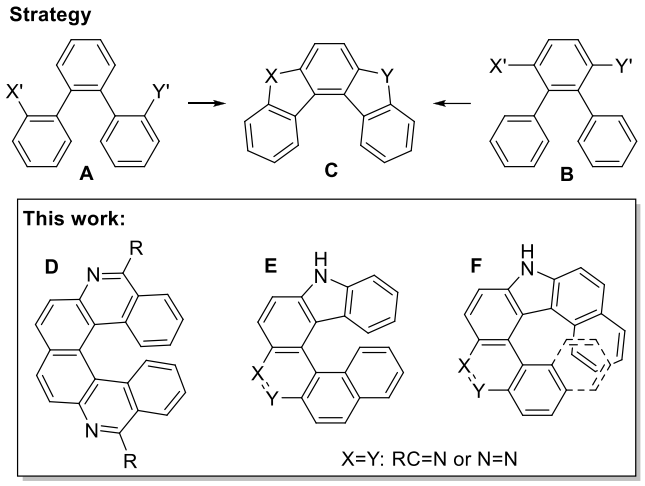

[a]Top: *ortho,ortho* fusion (X, Y, X′, and Y′ are suitable substituents and linkages); bottom: basic scaffolds of the helicenes synthesized by this approach.

These nitrogen-doped compounds offer a dynamic system where the photophysical and chiroptical properties can be selectively modulated. Crucially, we demonstrate that protonation-induced electronic reconfiguration leads to a significant response − including, in specific cases, a full sign inversion of the rotatory strength. By complementing the chiroptical characterization with density functional theory (DFT) calculations, we show that protonation induces a reorientation of the transition dipole moments. These insights position azahelicenes as promising candidates for pH-responsive biological probes or switchable emitters in organic light-emitting diodes (OLEDs).

RESULTS AND DISCUSSION

To evaluate the photophysical and chiroptical response of the aza-scaffolds upon protonation, we developed a divergent synthetic strategy enabling the modular assembly of various azahelicenes from common naphthyl precursors. The synthesis of 9*H*-benzo[4,5]indolo[2,3-*k*]phenanthridines **11** was initiated from commercially available 2-naphthol (**1**). This compound was first converted into 2-naphthylamine (**2**) via a *Bucherer* reaction,[16] which was subsequently iodinated at the 1-position using *N*-iodosuccinimide (NIS)[16b] to give the corresponding iodide **3** in an excellent 95% yield (Scheme 2). *Suzuki* coupling with 2-bromophenylboronic acid (**4**) afforded phenylnaphthalene **5** in 87% yield. Following a procedure reported by *Marten* et al., the amino group of this intermediate was transformed into the corresponding diazonium salt, which was subsequently substituted with sodium azide.[13d] The resulting azide **6** was obtained quantitatively and heated in *o*-xylene. This thermal activation generated a nitrene in situ[17] that underwent intramolecular C−H insertion[18] to furnish *ortho*-halogenated bromocarbazole **7**.[19] In the following step, this compound was coupled with 2-aminophenylboronic acid (**8**) under optimized *Suzuki* conditions. Reaction screening indicated that a combination of SPhos Pd G2 and SPhos in 1,4-dioxane/H_2O was highly effective, affording the coupling product **9** in an excellent yield of 96%. Subsequently, the amino group was converted into the corresponding amides **10** using both an aliphatic and an aromatic acid chloride, giving the products in high yields. Notably, the *Morgan-Walls* cyclization[20] with phosphoryl chloride in 1,2-dichlorobenzene proved to be highly robust; it enabled the efficient closure of the phenanthridine unit despite the increasing steric demand of the larger helical core. This allowed straightforward access to diaza[6]helicenes **11a** and **11b** with most satisfactory yields. Over the eight-step sequence, the *tert*-butyl-substituted hexahelicene **11a** was obtained in a total yield of 52%, while the phenyl-substituted analogue **11b** reached an overall yield of 48%.

Scheme 2. Synthesis of 9*H*-Benzo[4,5]indolo[2,3-*k*]phenanthridines

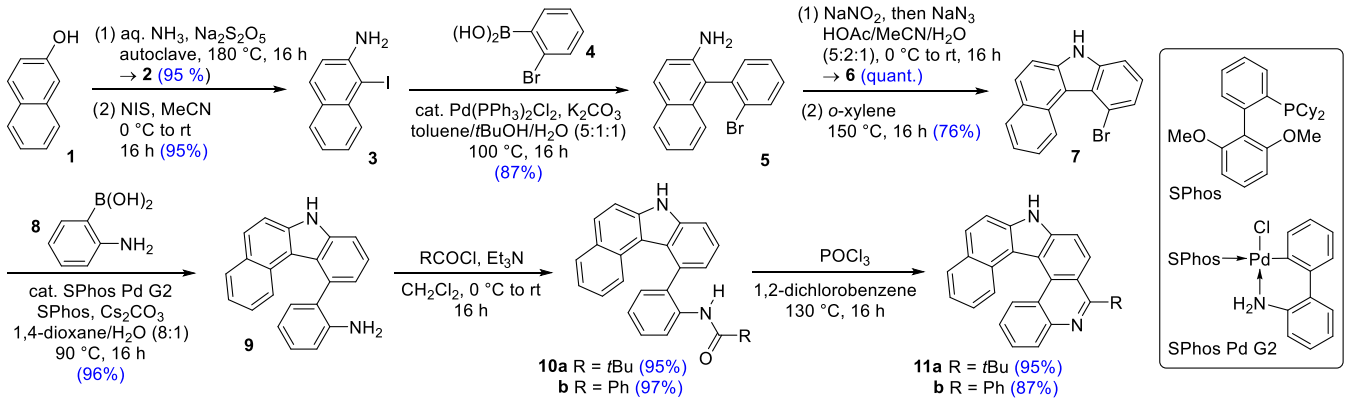

https://doi.org/10.1021/jacsau.6c00315
JACS Au XXXX, XXX, XXX−XXX

In addition to these compounds, two further constitutional isomers were obtained via a similar synthetic route (Scheme 3).

Scheme 3. Synthesis of 7*H*-Benzo[*a*]indolo[2,3-*k*]phenanthridines

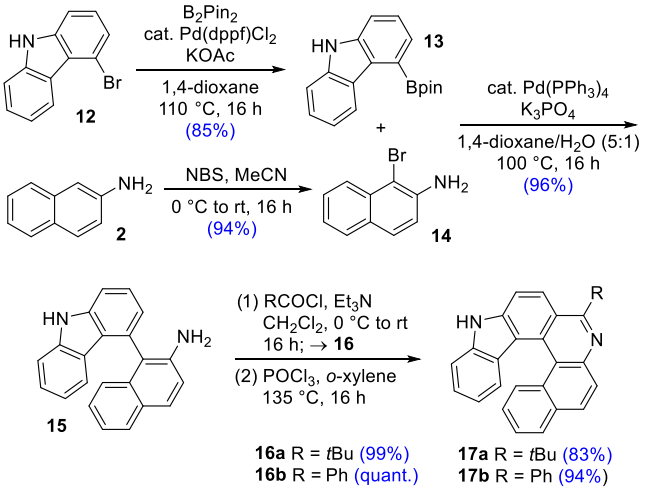

Following an approach reported by *Marten* et al.,[13d] 4-bromo-9*H*-carbazole (**12**) was borylated in a *Miyaura* reaction. While *Marten* and co-workers coupled the resulting boronate **13** with 2-aminophenylboronic acid (**8**) to access the corresponding diaza[5]helicenes,[13d] we instead performed the *Suzuki* coupling with 1-bromonaphthalen-2-amine (**14**), which was readily prepared from 2-naphthylamine (**2**). The resulting biaryl **15** was then converted into the corresponding amides **16** using the established methodology and subsequently cyclized to furnish diaza[6]helicenes **17a** and **b** in total yields of 67 and 77%, respectively, over four consecutive steps.

The two intermediately obtained aminobiaryls **9** and **15** similarly proved to be excellent substrates for the synthesis of cinnoline-containing azahelicenes (Scheme 4). Treatment of

Scheme 4. Synthesis of Benzocinnolinocarbazoles

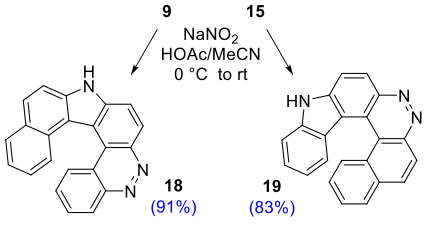

these amines with sodium nitrite, followed by gradual warming to room temperature, furnished the corresponding cinnolinocarbazoles **18** and **19** in 91% and 83% yield, respectively.

A significant synthetic challenge was encountered during the double *ortho* fusion starting from naphthalene-2,7-diol (**20**). Initial attempts to brominate the diamine **21** at the 1,8-positions exclusively yielded the undesired 3,8-dibromo isomer, regardless of the conditions tested. This regioselectivity issue, likely arising from the specific steric and electronic environment of the naphthalene core, necessitated an alternative strategy. To circumvent the steric shielding, we successfully implemented a chlorination using NCS to afford dichloride **22** in 89% yield (Scheme 5). However, the

Scheme 5. Synthesis of Phenanthridino[1,2-*a*]phenanthridines

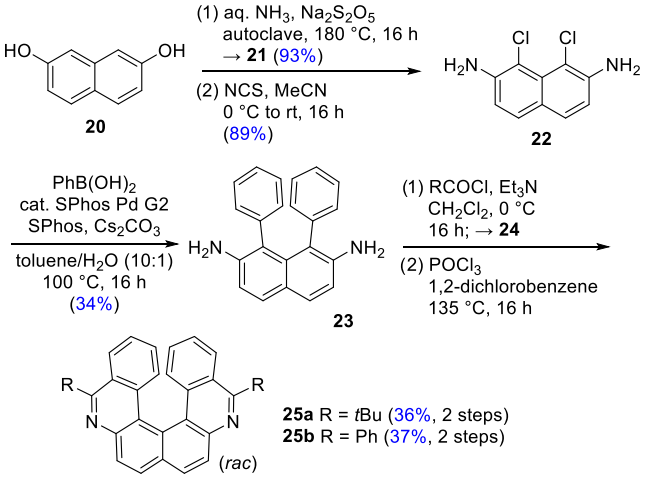

subsequent *Suzuki-Miyaura* coupling proved to be the bottleneck, as aryl chlorides are notoriously less reactive than their bromide counterparts. An extensive screening of catalyst/ligand systems was required to overcome this lack of reactivity. Ultimately, a combination of SPhos Pd G2 and cesium carbonate in a toluene/water mixture enabled the construction of the symmetric core **23**, albeit in a moderate yield of only 34%. The resulting diamine was subsequently acylated with pivaloyl chloride and benzoyl chloride, respectively, to afford the corresponding amides **24**, which were directly cyclized in *Morgan-Walls* reactions to furnish phenanthridino[1,2-*a*]-phenanthridines **25**.

To further demonstrate the scope of our synthetic strategy, we utilized diamine **23** to access 5,10-dihydrocarbazolo[3,4-*c*]carbazole (**27**). Although **27** is not amenable to protonation due to the absence of the phenanthridine motif, its synthesis illustrates the applicability of our strategy to more complex aza-architectures (Scheme 6). Following our established proce-

Scheme 6. Synthesis of Carbazolocarbazole

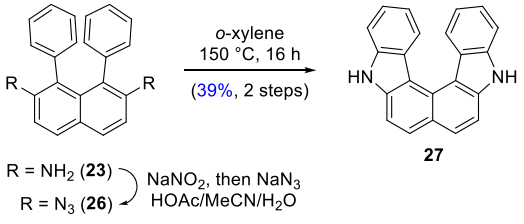

dure, **23** was converted into bis-azide **26** via diazotization and subsequent substitution. Thermal nitrene formation and intramolecular C−H insertion furnished the double carbazole framework. Although **27** was first reported by *Zander et al.* in 1969,[21] our route provides an efficient alternative to the established method. For example, *Liu* and co-workers obtained this compound in only 7% yield using modified *Bucherer* conditions.[22]

Coupling strategies toward larger helicenes starting from 1,8-dichloronaphthalene-2,7-diamine (**22**) were attempted using 1-naphthylboronic acid. Although the coupling product could be detected by mass spectrometry, it was never isolated in sufficient amounts. However, with the two building blocks 11-bromo-7*H*-benzo[*c*]carbazole (**7**) and 1-bromonaphthalen-2-

https://doi.org/10.1021/jacsau.6c00315
JACS Au XXXX, XXX, XXX−XXX

amine (**14**), suitable precursors were available enabling straightforward access to 7-helicenes. To this end, **7** was converted into the corresponding boronate **28** via *Miyaura* borylation, which was subsequently employed in a *Suzuki* coupling with naphthyl building block **14** (Scheme 7).

Scheme 7. Synthesis of 7*H*-Benzo[*a*]benzo[4,5]indolo[2,3-*k*]phenanthridines

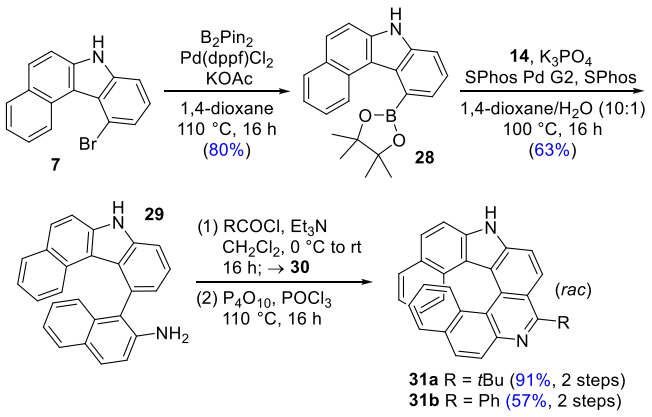

Boronate **28** was here obtained in an excellent 80% yield, while the coupling product from the *Suzuki* reaction (**29**) was isolated with a moderate yield of 60%. Amine **29** was converted into the corresponding amides **30** using the standard procedure with acid chlorides, which were then subjected without purification directly to *Morgan-Walls* reactions furnishing heptahelicenes **31a** and **b**.

Structural Properties of the Helicenes

Geometry optimizations were performed at the PBE0[23]/def2-TZVP[24] level including *Grimme*'s dispersion correction (D3)[25] with *Becke-Johnson* damping (GD3BJ)[26] for all obtained hexahelicenes, allowing the determination of structural parameters such as interplanar angles, the sum of torsion angles, and the distances between the centroids of the terminal rings. These parameters are summarized in Table 1. Further details of quantum-chemical calculations are given in the Supporting Information.

Helicenes **25a** and **25b** exhibit the largest interplanar angles of 52.9 and 50.6°, respectively, and also show the largest sums of torsion angles with 84.7 and 86.4°. In contrast, the various benzoindolophenanthridines **17a,b** and **11a,b** differ significantly with respect to these structural parameters. For example, *tert*-butyl-substituted derivatives **11a** and **17a** differ by 5.1° in their interplanar angles and by 5.3° in their sums of torsion angles. Values of a similar magnitude are observed when comparing phenyl-substituted derivatives **11b** and **17b**.

Table 1. Calculated Structural Properties of the Synthesized Hexa- and Heptahelicenes

compound	interplanar angle	sum of torsion angles	*d* [Å]
11a	45.6° (55.0°)[a]	61.7° (62.1°)[a]	4.98 (5.09)[a]
11b	45.7°	60.3°	5.03
17a	50.7° (56.2°)[a]	67.0° (66.5°)[a]	4.74 (4.85)[a]
17b	50.2°	66.1°	4.76
18	42.2°	58.5°	5.09
19	47.8°	63.4°	4.89
25a	52.9° (57.2°)[a]	84.7° (83.1°)[a]	4.35 (4.47)[a]
25b	50.6°	86.4°	4.32
27	43.0°	54.0°	5.31
31a	42.8 (51.1°)[a]	81.5 (75.8°)[a]	4.02 (4.27)[a]
31b	41.5	81.8	3.99

[a]Data in brackets from experimental XRD structures.

Crystals of the *tert*-butyl-substituted compounds were readily obtained by vapor-diffusion crystallization from the racemic solutions. Single-crystal X-ray diffraction was used to determine their structures where minor deviations from the computed solution-phase geometries were observed. Table 1 additionally summarizes some measured structural parameters from the X-ray analyses. Compound **11a** (CCDC-2513109) crystallizes in a triclinic system with space group $P\bar{1}$. The inversion center is clearly visible within the unit cell (Figure 1). Compound **25a** (CCDC-2513110) crystallizes analogously, while hexahelicene **17a** (CCDC-2513107) crystallizes in a monoclinic system with space group $P2_1/c$. Heptahelicene **31a** (CCDC-2513108) is of particular interest: It crystallizes as racemic conglomerate (where by chance a *P* crystal was picked for analyses) in an orthorhombic crystal system ($P2_12_12_1$).

These structural differences are also reflected in distinct racemization barriers, which were calculated for the parent scaffolds of all investigated helicenes. Based on these racemization barriers, half-lives of enantiomerization were determined using the *Eyring-Polanyi* equation. The transition states were calculated at the PBE0/def2-TZVP level using SCRF = (CPCM, solvent = dichloromethane) with empirical dispersion correction (GD3BJ). Frequency analyses revealed a single imaginary vibrational frequency, characteristic of a transition state. Exemplary IRC scans (Figure 2) further confirmed the nature of these transition states. After zero-point correction, lifetimes under standard conditions (298.15 K) were determined from the energy differences, and the corresponding half-lives were derived.

The parent scaffold of 7*H*-benzo[*a*]indolo[2,3-*k*]-phenanthridines (**17**, R = H) exhibits a racemization barrier of 115.7 kJ·mol^{-1}, which corresponds to a half-life of 1.3 years at 25 °C (Table 2). In comparison, the corresponding cinnoline **19** shows a shorter half-life and thus lower stability, attributable to helix expansion caused by the shorter N═N bond. Notably, a clear difference emerges between the 7*H*-benzo[*a*]indolo[2,3-*k*]phenanthridines **17** and the parent scaffold of the 9*H*-benzo[4,5]indolo[2,3-*k*]phenanthridines (**11**, R = H): In the latter, the racemization barrier is reduced by 22.6 kJ·mol^{-1}, shortening $t_{1/2}$ to only 1.2 days. Again, the cinnoline derivative **18** displays an even lower value. As expected, the parent scaffold of benzo[*a*]benzo[4,5]indolo[2,3-*k*]phenanthridines (**31**, R = H) exhibits the highest racemization barrier (154.0 kJ·mol^{-1}) owing to the seven fused aromatic rings. The corresponding half-life reaches approximately 8.4 millions of years. These results strongly suggest that phenanthridino[1,2-*a*]phenanthridines **25** and benzo[*a*]benzo[4,5]indolo[2,3-*k*]phenanthridines **31** can be separated into their enantiomers.

Basicity of the Azahelicenes

The nitrogen atoms within the phenanthridine units clearly exhibit basic properties. However, protonation behavior differs significantly in the investigated compounds, as demonstrated in particular by UV/vis titration experiments performed in CH_2Cl_2 (Figure 3). The most basic among the investigated compounds, **31a** (pK_a = 8.4, see Table 3 for pK_a values calculated with an aqueous solvent field), already exhibits a

https://doi.org/10.1021/jacsau.6c00315
JACS Au XXXX, XXX, XXX−XXX

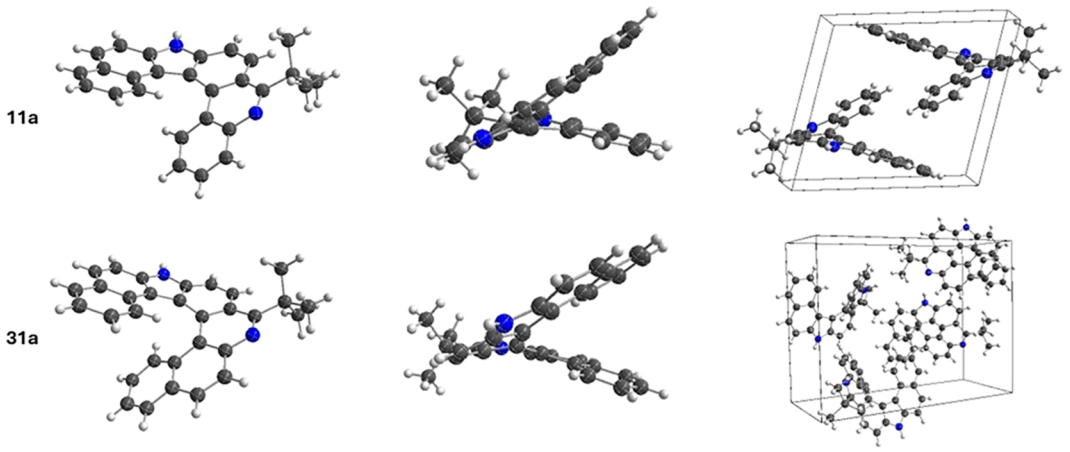

Figure 1. Crystal structures of hexahelicene **11a** (CCDC-2513109) and heptahelicene **31a** (CCDC-2513108) with different orientations together with the respective unit cells. Color code: carbon (black), nitrogen (blue), hydrogen (white). The structures of helicenes **17a** (CCDC-2513107) and **25a** (CCDC-2513110) are provided in the Supporting Information.

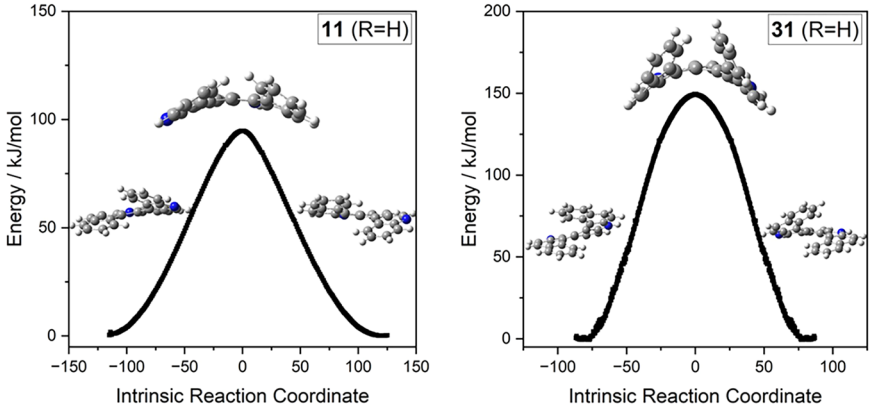

Figure 2. IRC calculations for hexahelicene **11** and heptahelicene **31**, confirming the connection between transition states and minima.

Table 2. Calculated Racemization Barriers and Half-Lives of Enantiomerization

core structure	E_a [kJ/mol]	$t_{1/2}$
11 (R = H)	93.1	1.2 d
17 (R = H)	115.7	1.3 a
18	89.6	0.3 d
19	108.9	30.3 d
25 (R = H)	146.0	$2.7{\cdot}10^5$ a
27	78.8	13.9 s
31 (R = H)	154.5	$8.4{\cdot}10^6$ a

pronounced shift in its absorption band even upon the addition of small amounts of TFA. The compound reaches complete saturation at addition of approximately ten equivalents, after which no further changes in the spectra are observed. In contrast, one of the less basic compounds **25b** (pK_a = 4.8), responds much more sluggishly: Incremental additions of TFA induce only gradual spectral evolution, with shifts persisting up to 200 equiv. This behavior is consistent with the presence of two basic pyridine-type nitrogen atoms in **25b**, which can be protonated in a stepwise fashion and thereby modulate the UV/vis response over a much broader pH range. The titration spectra of the other compounds are listed in the Supporting Information.

To gain deeper insight into the protonation behavior, pK_a values of the azahelicenes were calculated via DFT, applying a water solvent field (CPCM). For this purpose, the proton exchange method was employed,[27] in which solvent-dependent free energies of the compounds are correlated with the experimental pK_a value of phenanthridinium (pK_a = 4.47 in H_2O)[28] as reference according to the following equation

$$pK_a\,(B{-}H^+) = \frac{\Delta G^*_{solv}}{RT\ln(10)} + pK_a\,(ref{-}H^+)$$

Calculated pK_a values of the compounds are summarized in Table 3.

The reversibility of the protonation−deprotonation process, which qualifies these molecules as robust molecular switches, was investigated using compound **31a** (see Figure 4). The compound was subjected to ten consecutive switching cycles. A wavelength of 356 nm was selected for monitoring, as it represents the point of maximum absorbance change upon protonation (c.f., Figure 3). To ensure accuracy, the absorbance values were corrected for the cumulative dilution resulting from the sequential addition of acid (TFA) and base (Et_3N). The data show good stability over ten consecutive cycles, with no significant degradation of the absorbance signal.

Photophysical and Chiroptic Characterization of Hexa- and Heptahelicenes

The herein synthesized hexahelicenes were characterized by UV/vis and fluorescence spectroscopy. Protonation of these compounds is possible due to the basic properties of the

https://doi.org/10.1021/jacsau.6c00315
JACS Au XXXX, XXX, XXX−XXX

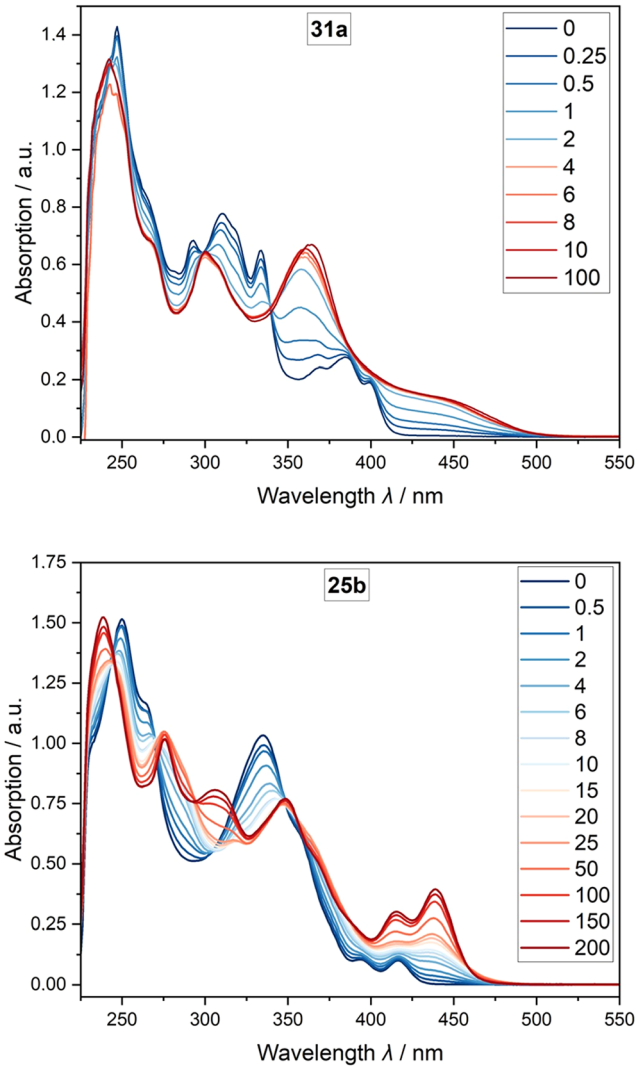

Figure 3. UV/vis spectra of heptahelicene **31a** and hexahelicene **25b** measured in CH_2Cl_2 in the presence of increasing amounts of TFA.

Table 3. Calculated pK_a Values of the Helicenes (CPCM, H_2O)

compound	pK_a	compound	pK_a
11a	8.2	**11b**	7.3
17a	8.3	**17b**	6.9
18	4.4	**19**	5.0
25a	5.7	**25b**	4.8
31a	8.4	**31b**	7.2

nitrogen atoms within the respective phenanthridine motifs. The observed pronounced spectral changes upon protonation render these compounds intriguing candidates for reversibly protonatable systems.[29] In addition, fluorescence quantum yields were determined for all target compounds. All spectroscopic measurements were carried out in CH_2Cl_2 at 20 °C. An excitation wavelength of 330 nm was used consistently for fluorescence experiments including the determination of fluorescence quantum yields. Figure 5 displays the absorption and fluorescence spectra as well as the corresponding spectra after protonation by addition of trifluoroacetic acid (TFA) for a selection of the helicenes.

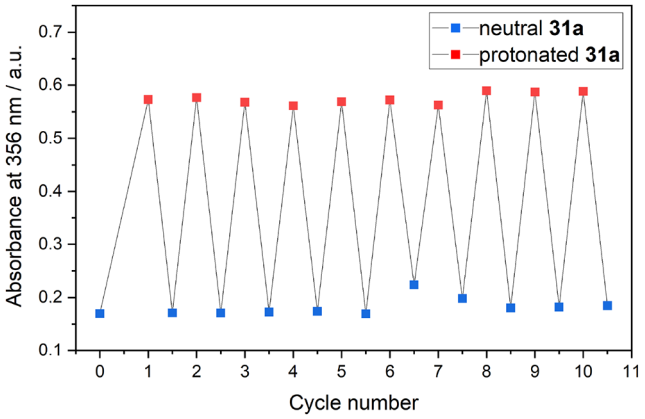

Figure 4. Investigation of the protonation−deprotonation process using UV/vis spectroscopy.

Spectra of the further investigated compounds are given in the Supporting Information.

Overall, the absorption characteristics of all compounds are quite similar, and their molar extinction coefficients fall within the same order of magnitude; regions of strong absorptions are essentially in the range of 4−5 × 10^4 L·mol^{-1}·cm^{-1}. Time-dependent DFT (TD-DFT) calculations allowed assignment of the observed absorption bands to the respective electronic transitions. The intense absorption features can essentially be attributed to HOMO−1 → LUMO and HOMO → LUMO+1 transitions, while the energetically lowest absorptions with weak oscillator strength correspond, as expected, to HOMO → LUMO transitions. A more detailed listing of transitions is provided in the Supporting Information.

Computational results (Table 4) confirm the expectation that HOMO−LUMO gaps narrow as the aromatic system extends. Accordingly, the two [7]helicenes, **31a** and **31b**, exhibit the smallest gaps (4.02 and 4.00 eV, respectively), excluding the cinnoline derivative **18**. For the [6]helicenes, the values range between 4.10 and 4.23 eV. These HOMO−LUMO gaps correlate well with the lowest energy absorption maxima: For the [7]helicenes, these are observed at 385 and 389 nm, both displaying a characteristic shoulder at longer wavelengths.

The investigated compounds allow for the derivation of insightful structure−property relationships, discussed here for the *tert*-butyl-substituted derivatives. *Marten et al.* recently reported an analogously substituted indolo[2,3-*k*]phenanthridine (a [5]helicene) with a HOMO−LUMO gap of 4.61 eV.[13d] The [6]helicenes **11a** and **17a** differ from this reference only by the site of the additional benzene ring fusion (either at the carbazole or phenanthridine moiety). Extending the aromatic system on the phenanthridine site (**17a**) reduces the HOMO−LUMO gap by 0.33 eV. Conversely, extending the carbazole site yields a more pronounced conjugation effect with 0.47 eV reduction of the HOMO−LUMO gap. The further transition from [6]- to [7]helicene decreases the gap by only 0.12 eV, which can be attributed to increased torsional strain within the aromatic backbone, thereby limiting further gains in conjugation. Upon protonation, the HOMO−LUMO gap decreases significantly (by 0.38−0.99 eV), resulting in a consistent bathochromic shift across all absorption spectra. In addition to the frontier orbital gaps, the singlet (S_1) and triplet (T_1) excited-state energies and their corresponding $\Delta(S_1-T_1)$ gaps were calculated. These gaps range from 0.71 to 0.94 eV,

https://doi.org/10.1021/jacsau.6c00315
JACS Au XXXX, XXX, XXX−XXX

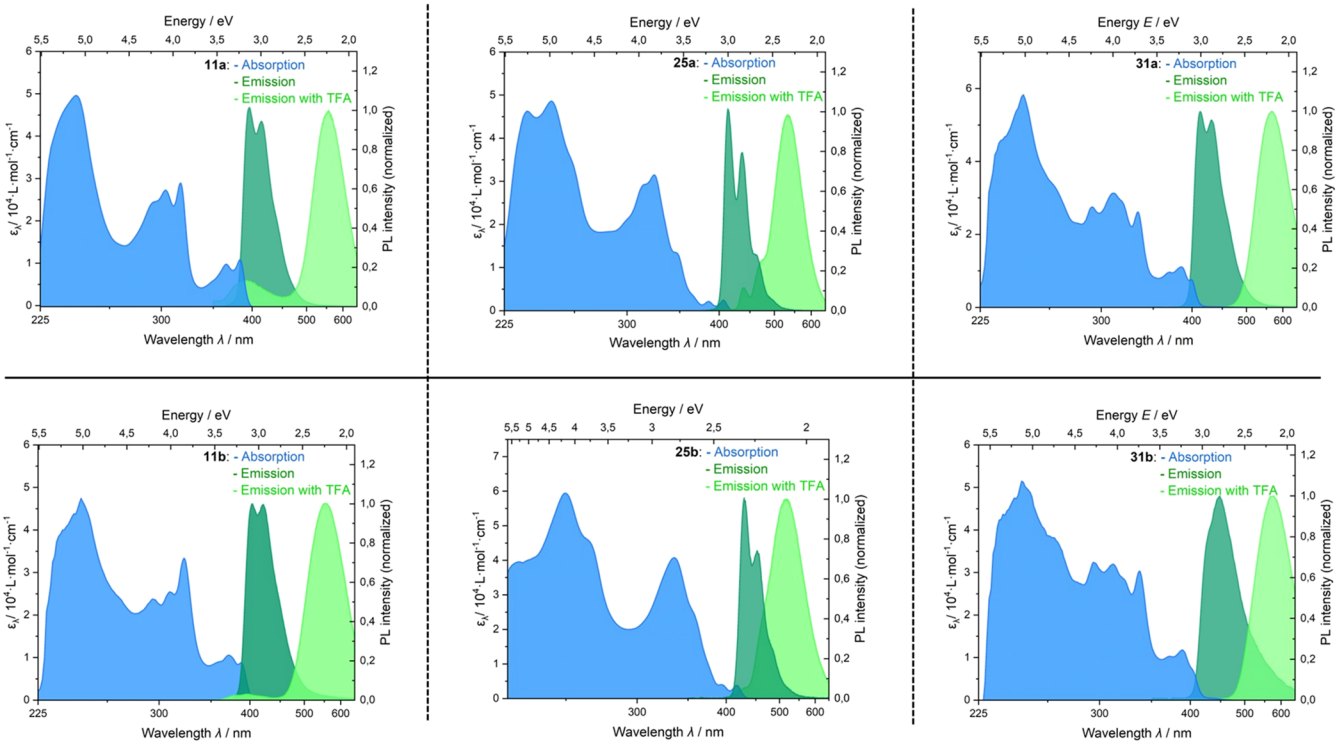

Figure 5. Absorption (blue) and fluorescence (green) spectra of representative helicenes measured in CH_2Cl_2 at 20 °C. Fluorescence spectra after addition of TFA (light green; 25 eq, or 50 eq for **25a** and **25b**) were recorded under the same conditions. Data for all further compounds are given in the Supporting Information.

Table 4. Electronic and Photophysical Properties

compound	λ_{max} (abs)[a] [nm]	λ_{max} (em)[a] [nm]	$\Delta\lambda$ (em)[a]/ΔE (em)[a] [nm]/[eV]	Δ (HOMO−LUMO)[b] [eV]	S_1[b] [eV]	T_1[b] [eV]	Δ (S_1−T_1)[b] [eV]	PLQY (σ)[a] [%]
11a	315, 383	396, 414	151/0.98[c]	4.14	3.11	2.28	0.83	27.7 (1.8)
11a·H^+	348	556		3.60	2.58	2.09	0.48	9.7 (0.2)
11b	322, 372	404, 421	138/0.75[c]	4.10	3.08	2.28	0.80	12.1 (0.8)
11b·H^+	355	550		3.43	2.41	1.99	0.42	3.74 (0.3)
17a	312	418	57/0.36	4.28	3.20	2.33	0.88	3.4 (1.7)
17a·H^+	338, 410	475		3.99	2.89	2.28	0.61	10.2 (1.5)
17b	318	468	23/0.12	4.21	3.11	2.23	0.88	<1%
17b·H^+	338, 409	491		3.83	2.71	2.16	0.54	7.1 (1.2)
18	335, 372	496	38/0.17	3.98	2.81	2.03	0.78	<1%
18·H^+	365, 439	534		2.99	1.97	1.57	0.40	<1%
19	325, 389	452	103/0.51	4.13	2.82	2.11	0.71	<1%
19·H^+	349, 455	555		3.48	2.41	1.84	0.57	1.9 (1.0)
25a	323	413, 436	90/0.52[c]	4.23	3.18	2.30	0.88	3.2 (0.8)
25a·H^+	409, 432	513		3.65	2.53	2.13	0.40	15.0 (1.8)
25b	336	429, 453	76/0.42[c]	4.10	2.95	2.12	0.83	<1%
25b·H^+	347, 414, 439	515		3.42	2.35	2.02	0.33	15.7 (0.6)
27	314	379, 398		4.36	3.34	2.40	0.94	12.7 (0.2)
31a	310, 334, 385	412, 431	144/0.75[c]	4.02	2.98	2.22	0.76	29.7 (2.1)
31a·H^+	363	565		3.56	2.55	2.06	0.49	8.1 (0.1)
31b	312, 338, 389	444	126/0.62	4.00	2.97	2.23	0.74	4.6 (0.1)
31b·H^+	358	570		3.41	2.39	1.97	0.43	4.7 (0.2)

[a]Measured data. [b]Obtained from quantum-chemical calculations. [c]Difference calculated from the weighted average of the two emission maxima.

mirroring the conjugation effects previously discussed for the HOMO−LUMO transitions. Consistent with these observations, protonation of the compounds leads to a further narrowing of the energy gaps. This process also exerts a significant influence on the photophysical properties; specifically, the fluorescence spectra exhibit a pronounced bathochromic shift upon protonation. Molecular orbital analysis reveals that these transitions are mostly due to intramolecular charge-transfer, evidenced by the spatial separation between the respective HOMOs and LUMOs in the protonated species. The frontier molecular orbitals are depicted in the Supporting Information.

https://doi.org/10.1021/jacsau.6c00315
JACS Au XXXX, XXX, XXX−XXX

Among all characterized compounds, *tert*-butyl-substituted 9*H*-benzo[4,5]indolo[2,3-*k*]phenanthridine **11a** exhibits the largest bathochromic shift of 151 nm (0.98 eV). A comparable shift is observed for its phenyl-substituted analogue **11b**. 7-Helicenes **31a** and **b** display similarly large shifts, amounting to 144 nm (0.75 eV) for *tert*-butyl derivative **31a** and 126 nm (0.62 eV) for its phenyl-substituted analogue **31b**. In contrast, phenanthridino[1,2-*a*]phenanthridines **25a** and **b** show considerably smaller shifts of 90 nm (0.52 eV) and 76 nm (0.42 eV), respectively. Notably, *tert*-butyl substitution consistently leads to more pronounced bathochromic shifts. This trend is also evident for 7*H*-benzo[*a*]indolo[2,3-*k*]phenanthridines **17a** and **b**, which display the smallest bathochromic shifts of only 57 and 23 nm (0.36 and 0.12 eV), respectively. In addition to these variably pronounced bathochromic shifts, another remarkable feature was observed for these compounds upon protonation: a significant change in the photoluminescence quantum yields (PLQY, Table 4). PLQYs of the helicenes were determined in CH_2Cl_2 using an integrating sphere. The reported values represent the average of three independent measurements. Compound **17a** displayed a PLQY of 3%, which is a typical value for helicenes. However, protonation resulted in a 3-fold increase of the fluorescence quantum yield. Phenyl-substituted isomer **17b** was nonemissive in its neutral state but exhibited a similar fluorescence enhancement upon protonation. A comparison with the constitutional isomers **11a** and **11b** which only differ in the position of the terminal *ortho*-fused benzene ring, is particularly revealing. The neutral form of **11a** showed a remarkably high PLQY of 28%, an impressive value for the notoriously weakly emissive helicenes. For the extended heptahelicenes based on the same benzo[4,5]indolo-[2,3-*k*]phenanthridine framework (**11a** and **11b**), even higher fluorescence quantum yields were observed. *tert*-Butyl-substituted derivative **31a** exhibited a considerable PLQY of 30%, whereas its phenyl-substituted analogue **31b** showed a significantly lower value of 4.6%. Upon protonation, however, its quantum yield decreased − a trend, similarly observed for the respective phenyl-substituted analogue **31b**. In general, *tert*-butyl-substituted derivatives exhibit fluorescence quantum yields several times higher than their phenyl-substituted counterparts. The phenanthridino[1,2-*a*]phenanthridines displayed a similar behavior: A PLQY of 3% was determined for the more strongly emissive compound **25a**, while protonation led to a 5-fold increased value. Even helicene **25b**, which is almost nonemissive in its neutral state, showed a remarkable 26-fold enhancement of its fluorescence quantum yield upon protonation. In contrast, the cinnoline derivatives exhibited negligible fluorescence, with photoluminescence quantum yields falling below 2% in both their neutral and protonated states. Nitrogen-containing heterocycles such as quinolines are known to exhibit substantially lower fluorescence efficiencies compared to their isoelectronic hydrocarbons.[29a] This behavior is attributed to n,π^* transitions from nonbonding electrons, which enhance spin−orbit coupling and thus promote intersystem crossing, ultimately reducing fluorescence quantum yields.[29a,30]

It seems quite obvious that the increase in fluorescence upon protonation, which was observed for some of the investigated helicenes is due to the nitrogen lone pair. According to *Tervola et al.*, the excited S_1 state is converted by protonation into a π,π^* state. These exhibit shorter radiative lifetimes, thereby increasing the likelihood of fluorescence at the expense of intersystem crossing.[11a,29a,31] Conversely, in helicenes that exhibit relative strong fluorescence in their neutral states, protonation of the nitrogen atom impedes the lone pair's delocalization and thus alters the nature of the excited state. This promotes nonradiative decay pathways such as an intersystem crossing or internal conversion and leads to a pronounced quenching of fluorescence in the protonated helicenes.

To further evaluate the electronic properties, cyclic voltammetry (CV) was performed on two representative derivatives (**25a** and **31a**); the resulting voltammograms and a brief discussion is provided in the Supporting Information (Section 7).

To investigate the chiroptical properties of the helicenes, those with a sufficiently high racemization barrier were separated by chiral HPLC (Supporting Information). Only helicenes **31a**, **31b**, and **25b** could be resolved. The corresponding *tert*-butyl-substituted analogue **25a** could not be separated into enantiomers under the available chromatographic conditions, and the two enantiomers invariably coeluted. The resolved fractions were assigned to the respective enantiomers based on their ECD spectra, supported by TD-DFT calculations.

The ECD spectrum of compound **31a** is given in Figure 6. Comparison with quantum-chemical calculations revealed that

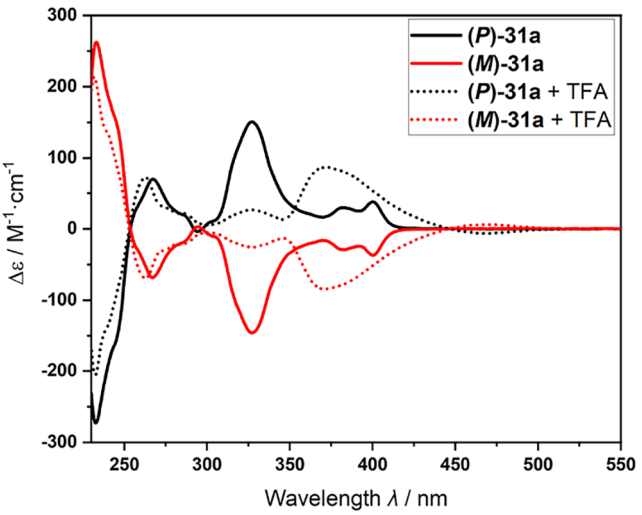

Figure 6. ECD spectra of the enantiomers of **31a** in the neutral and in the protonated state. (A magnified section is given in the Supporting Information.)

the first-eluted enantiomer corresponds to the *P* enantiomer, while the *M* enantiomer was eluted subsequently (see Supporting Information). As expected, the enantiomers give rise to identical but mirror-image spectra. The effect of protonation was also examined. Similar to the UV/vis spectrum, a red-shift is observed in the ECD spectra upon addition of 25 equiv of TFA. For the first $S_0 \rightarrow S_1$ transition of **31a**, the g_{abs} value in the neutral form is 6×10^{-3}, decreasing to 1.5×10^{-3} upon protonation.

Beyond their absorption properties, the luminescence behavior of the compounds was examined. Figure 7 presents the emission spectrum of compound **31a** as a representative example, while the remaining spectra are provided in the Supporting Information. The g_{lum} values were extracted from the CPL spectra and are listed in Table 5 together with the corresponding g_{abs} values.

https://doi.org/10.1021/jacsau.6c00315
JACS Au XXXX, XXX, XXX−XXX

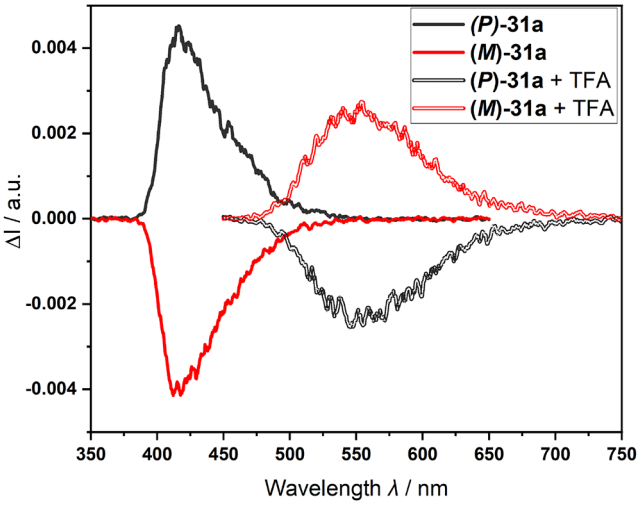

Figure 7. CPL spectra of the enantiomers of **31a** in the neutral and in the protonated states.

Table 5. Absorption and Luminescence Dissymmetry Factors and Brightness of CPL

compound	g_{abs}	g_{lum}	$\varepsilon_{(330\ nm)}$ ($M^{-1}\cdot cm^{-1}$)	B_{CPL}
25b	3×10^{-4}	no signal	39 300	–
25b·H^+	2×10^{-4}	6×10^{-4}	24 700	1.2
31a	6×10^{-3}	3.5×10^{-3}	23 400	12.2
31a·H^+	1.5×10^{-3}	2.5×10^{-3}	16 100	1.6
31b	4×10^{-3}	2×10^{-3}[a]	25 000	1.2
31b·H^+	1×10^{-3}	no signal	19 500	–

[a] 6×10^{-4} in the area of 525–550 nm.

The helicenes exhibit typical g_{abs} and g_{lum} values, which are generally reported in the literature to be in the range of 10^{-2} to 10^{-4}. The highest g_{abs} value was observed for compound **31a**. Addition of TFA results in a decrease of the absorption g factors for the protonated species by a factor of 1.5 to 4, depending on the compound. For luminescence, g factors were measured in the range of 3.5×10^{-3} to 6×10^{-4}. Due to the low signal intensity, it was not possible to determine g factors for all compounds.

To provide a comprehensive assessment of the chiral luminescence performance, the brightness of CPL (B_{CPL}) was calculated in both their neutral and protonated states according to the following equation[32]

$$B_{CPL} = \varepsilon_{(\lambda\ exc)} \cdot \Phi_{PLQY} \cdot 0.5 |g_{lum}|$$

where $\varepsilon_{(\lambda\ exc)}$ is the molar extinction coefficient at the excitation wavelength and Φ_{PLQY} the fluorescence quantum yield (c.f., Table 4). The data are given in Table 5.

Figure 7 not only shows a modulation of g_{lum} upon protonation of **31a**. It furthermore demonstrates a striking inversion of the luminescence dissymmetry factor g_{lum}, which has occasionally been observed for nitrogen-containing helicenes.[10b,33] To elucidate this phenomenon from a physicochemical perspective,[34] g_{lum} can be expressed as

$$g_{lum} = 4 \times \frac{R}{D}$$

where R represents the rotatory strength and D denotes the dipole strength. The dipole strength D is defined as the squared of the electronic transition dipole moment μ for the transition between the excited-state wave function Ψ_j and the ground-state wave function Ψ_i

$$D = \langle \Psi_j | \mu | \Psi_i \rangle^2$$

The rotatory strength R, which dictates the sign and intensity of the chiroptical signal, is determined by the scalar product of the electronic (μ) and magnetic (m) transition dipole moments

$$R = lm[\langle \Psi_j | \mu | \Psi_i \rangle \times \langle \Psi_j | m | \Psi_i \rangle] = |\mu| \times |m| \cos \varphi_{\mu,m}$$

where lm refers to an imaginary component of the scalar product. In this expression, $\varphi_{\mu,m}$ represents the angle between the electric and magnetic transition dipole moment vectors. This relationship demonstrates that a sign inversion of R (and thus of g_{lum}) can be triggered by a significant reorientation of the transition dipole moments – specifically when the angle $\varphi_{\mu,m}$ crosses the 90° threshold.

Both R and D can be obtained from TD-DFT calculations of the S_1 state, such that the sign reversal of the experimental g factor can be substantiated by quantum-mechanical calculations (Table 6). For compound **31a**, upon protonation of the

Table 6. Calculated Rotatory Strength and Dipole Strength of the First Transition ($S_1 \rightarrow S_0$)

compound	D/a.u.	R/cgs [P/M]
25b	9.66	−111/+111
25b·H^+	2.19	−40/+40
31a	5.58	+253/−253
31a·H^+	1.41	−63/+63
31b	6.18	+91/−91
31b·H^+	1.97	−70/+70

P enantiomer, the rotatory strength changes sign from $+253 \times 10^{-40}$ to -63×10^{-40} erg·esu·cm/Gauss accompanied by a decrease in magnitude. Conversely, the M enantiomer exhibits the opposite behavior.

To provide a more intuitive understanding of the chiroptical response, we analyzed the orientation of the electric (μ, blue) and magnetic (m, red) transition dipole moment vectors for the $S_1 \rightarrow S_0$ transition (Figure 8). As the rotatory strength R is proportional to cos $\varphi_{\mu,m}$, the sign of the chiroptical signal is governed by the relative angle between these two vectors. Visual inspection reveals that protonation induces a significant reorientation of both transition dipole moments. Crucially, in

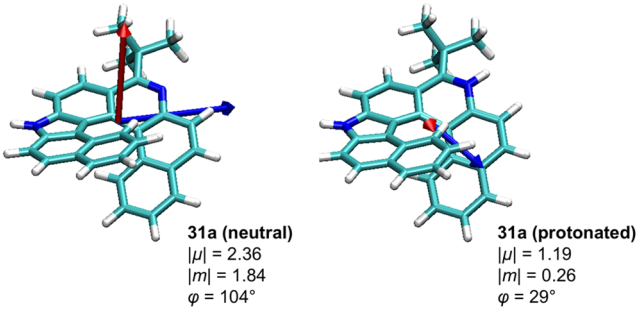

Figure 8. Calculated electric (μ, blue) and magnetic (m, red) transition dipole moment vectors (in atomic units, a.u.) for neutral and protonated **31a**. The inversion of the CPL signature is rationalized by a reorientation of the vectors across the 90° threshold.

https://doi.org/10.1021/jacsau.6c00315
JACS Au XXXX, XXX, XXX–XXX

the case of **31a**, this redirection causes the angle $\varphi_{\mu,m}$ to shift across the 90° threshold (e.g., from an acute to an obtuse angle), which mathematically accounts for the observed sign reversal of *R*. Furthermore, the calculations show a decrease in the magnitudes of both vectors upon protonation − with a particularly pronounced reduction in the magnetic transition dipole moment − consistent with the diminished *R* and *D* values summarized in Table 6.

Compound **31b** similarly exhibits a reversal of the rotatory strength upon protonation. A direct comparison with experimental data is precluded, however, as the resulting CPL signal was below the detection threshold. Nevertheless, a closer inspection of the ECD spectrum (see Supporting Information) reveals that, alongside the spectral shift and reduced intensity, a sign inversion occurs, which is consistent with the rotatory strengths obtained from TD-DFT calculations at the ground-state geometry.

TD-DFT calculations further indicate that compound **25b** does not undergo a *g*-factor inversion upon protonation, a finding corroborated by experimental ECD spectra where no sign reversal is observed. This behavior is further elucidated by the analysis of the transition dipole moments: In contrast to the **31** series, **25b** exhibits no significant angular shift across the 90° threshold between the electric and magnetic transition dipole moment vectors (Figure 9).

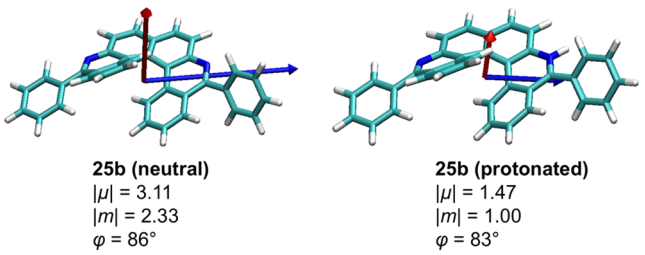

Figure 9. Calculated electric (μ, blue) and magnetic (m, red) transition dipole moment vectors (in atomic units, a.u.) for neutral and protonated **25b**. In contrast to **31a**, the angle between the vectors remains nearly constant.

Consequently, the chiroptical response remains qualitatively invariant, as the relative orientation of the transition moments is preserved upon protonation. The visualization of the transition dipole moments for all other synthesized derivatives is provided in the Supporting Information. Notably, in addition to the **31** series, the derivatives of series **11** also exhibit an angular shift across the 90° threshold upon protonation.

CONCLUSION

In summary, we have successfully expanded our modular synthetic approach to include ten novel aza[6]- and [7]-helicenes starting from readily accessible precursors. All compounds were systematically characterized, revealing remarkably high fluorescence quantum yields for helicene architectures, reaching 30% for the *tert*-butyl-substituted indolo[2,3-*k*]phenanthridine derivatives. Furthermore, reversible protonation induced significant bathochromic shifts of up to 151 nm (0.98 eV), accompanied by substantial changes in emission intensity. These experimental data were complemented by DFT calculations of the frontier molecular orbitals and the singlet and triplet excited states. In addition, the transition states for racemization were calculated. The phenanthridino[1,2-*a*]phenanthridines and 7*H*-benzo[*a*]-benzo[4,5]indolo[2,3-*k*]phenanthridine exhibit barriers exceeding 145 kJ/mol, enabling the successful enantiomeric separation of three compounds via chiral HPLC. Chiroptical characterization via ECD and CPL spectroscopy revealed g_{lum} values of up to 3.5×10^{-3}. Most significantly, for the [7]helicene derivatives, reversible protonation triggered an inversion of the CPL signature, albeit with a concomitant decrease in intensity. This experimental behavior was corroborated by TD-DFT calculations, which confirmed a reversal of the rotatory strength arising from a change in the angle between electric and magnetic transition dipole moments. Consequently, these [7]helicenes represent promising candidates for further research into high quantum yield emitters with significant dissymmetry factors, as well as for potential applications in stimuli-responsive photonics.

ASSOCIATED CONTENT

Supporting Information

The Supporting Information is available free of charge at https://pubs.acs.org/doi/10.1021/jacsau.6c00315.

Experimental procedures; spectroscopic data; NMR spectra; details of optophysical investigations; and quantum-chemical calculations (PDF)

Accession Codes

Deposition Numbers 2513107 (**17a**), 2513108 (**31a**), 2513109 (**11a**), and 2513110 (**25a**) contain the supplementary crystallographic data for this paper. These data can be obtained free of charge via the joint Cambridge Crystallographic Data Centre (CCDC) and Fachinformationszentrum Karlsruhe Access Structures service.

AUTHOR INFORMATION

Corresponding Author

Joachim Podlech − *Institute for Organic Chemistry, Karlsruhe Institute of Technology (KIT), 76131 Karlsruhe, Germany;* orcid.org/0000-0001-7881-6905;
Email: joachim.podlech@kit.edu

Authors

Felix R. Schumann − *Institute for Organic Chemistry, Karlsruhe Institute of Technology (KIT), 76131 Karlsruhe, Germany*

Clotilde Philippe − *University of Rennes, CNRS, ISCR-UMR 6226, Rennes 35000, France*

Pascal Weisenburger − *Institute for Inorganic Chemistry, Karlsruhe Institute of Technology (KIT), 76131 Karlsruhe, Germany*

Jeanne Crassous − *University of Rennes, CNRS, ISCR-UMR 6226, Rennes 35000, France;* orcid.org/0000-0002-4037-6067

Complete contact information is available at: https://pubs.acs.org/10.1021/jacsau.6c00315

Author Contributions

CRediT: **Felix R. Schumann** conceptualization, investigation, methodology, writing - original draft, writing - review & editing; **Clotilde Philippe** investigation, writing - review & editing; **Pascal Weisenburger** investigation, writing - review & editing; **Jeanne Crassous** investigation, resources, writing - review & editing; **Joachim Podlech** conceptualization, project

https://doi.org/10.1021/jacsau.6c00315
JACS Au XXXX, XXX, XXX−XXX

administration, supervision, writing - original draft, writing - review & editing.

Funding

German Research Foundation (DFG): INST 40/575−1 FUGG (JUSTUS 2 cluster); French National Agency: ANR projects LumoMat-E, 18-EURE-0012.

Notes

The authors declare no competing financial interest.

■ ACKNOWLEDGMENTS

We are deeply grateful to Prof. Dirk Menche and Andreas Schneider (University of Bonn) for their generous support and expert guidance in the enantiomeric separation of helicenes using chiral HPLC. Furthermore, we sincerely thank Prof. Dr. H.-A. Wagenknecht (Institute of Organic Chemistry, Karlsruhe Institute of Technology, KIT) for providing access to a fluorimeter, and Prof. Dr. F. Breher (Institute of Inorganic Chemistry, Karlsruhe Institute of Technology, KIT) for giving access to an X-ray diffractometer and the equipment for CV measurements. The authors acknowledge support by the state of Baden-Württemberg through bwHPC and the German Research Foundation (DFG) through grant no INST 40/575-1 FUGG (JUSTUS 2 cluster). F.R.S. gratefully acknowledges financial support from the Stiftung der Deutschen Wirtschaft (sdw). P.W. thanks the Fonds der Chemischen Industrie for a Kekulé scholarship. C.P. and J.C. acknowledge the Ministère de la Recherche et de l'Enseignement Supérieur, the Centre national de la recherche scientifique (CNRS), and the French National Agency (ANR projects LumoMat-E, 18-EURE-0012).

■ ABBREVIATIONS

CPL, circularly polarized luminescence; CV, cyclic voltammetry; dppf, 1,1′-bis(diphenylphosphino)ferrocene; ECD, electronic circular dichroism; NBS, *N*-bromosuccinimide; NCS, *N*-chlorosuccinimide; NIS, *N*-iodosuccinimide; Pin, pinacolato; PLQY, photoluminescence quantum yield; SPhos, dicyclohexyl(2′,6′-dimethoxy[1′,1′-biphenyl]-2-yl)phosphane; SPhos, Pd G2 chloro(2-dicyclohexylphosphino-2′,6′-dimethoxy-1,1′-biphenyl)[2-(2′-amino-1,1′-biphenyl)]palladium(II); TFA, trifluoroacetic acid

■ REFERENCES

(1) (a) Gingras, M. One Hundred Years of Helicene Chemistry. Part 1: Non-Stereoselective Syntheses of Carbohelicenes. *Chem. Soc. Rev.* **2013**, *42* (3), 968−1006. (b) Gingras, M.; Félix, G.; Peresutti, R. One Hundred Years of Helicene Chemistry. Part 2: Stereoselective Syntheses and Chiral Separations of Carbohelicenes. *Chem. Soc. Rev.* **2013**, *42* (3), 1007−1050. (c) Gingras, M. One Hundred Years of Helicene Chemistry. Part 3: Applications and Properties of Carbohelicenes. *Chem. Soc. Rev.* **2013**, *42* (3), 1051−1095.

(2) (a) Grimme, S.; Peyerimhoff, S. D. Theoretical Study of the Structures and Racemization Barriers of [*n*]Helicenes (*n* = 3−6, 8). *Chem. Phys.* **1996**, *204* (2), 411−417. (b) Janke, R. H.; Haufe, G.; Würthwein, E.-U.; Borkent, J. H. Racemization Barriers of Helicenes: A Computational Study. *J. Am. Chem. Soc.* **1996**, *118* (25), 6031−6035. (c) Barroso, J.; Cabellos, J. L.; Pan, S.; Murillo, F.; Zarate, X.; Fernandez-Herrera, M. A.; Merino, G. Revisiting the Racemization Mechanism of Helicenes. *Chem. Commun.* **2018**, *54* (2), 188−191.

(3) (a) Zhao, W.-L.; Li, M.; Lu, H.-Y.; Chen, C.-F. Advances in Helicene Derivatives with Circularly Polarized Luminescence. *Chem. Commun.* **2019**, *55* (92), 13793−13803. (b) Abbate, S.; Longhi, G.; Mori, T. Chiroptical Properties of Helicenes. Historical Perspective and Structure-Property Relationships. In *Helicenes. Synthesis, Properties, and Applications*; Crassous, J.; Stará, I. G.; Starý, I. Eds.; Wiley-VCH, 2022; pp 373−394. (c) Qiu, M.; Du, J.; Yao, N.-T.; Wang, X.-Y.; Gong, H.-Y. Advances in Nitrogen-Containing Helicenes: Synthesis, Chiroptical Properties, and Optoelectronic Applications. *Beilstein J. Org. Chem.* **2025**, *21*, 1422−1453. (d) Maeda, C.; Ema, T. Recent Development of Azahelicenes Showing Circularly Polarized Luminescence. *Chem. Commun.* **2025**, *61* (25), 4757−4773.

(4) (a) Brandt, J. R.; Wang, X.; Yang, Y.; Campbell, A. J.; Fuchter, M. J. Circularly Polarized Phosphorescent Electroluminescence with a High Dissymmetry Factor from PHOLEDs Based on a Platinahelicene. *J. Am. Chem. Soc.* **2016**, *138* (31), 9743−9746. (b) Lin, Y.-S.; Abate, S. Y.; Lai, K.-W.; Chu, C.-W.; Lin, Y.-D.; Tao, Y.-T.; Sun, S.-S. New Helicene-Type Hole-Transporting Molecules for High-Performance and Durable Perovskite Solar Cells. *ACS Appl. Mater. Interfaces* **2018**, *10* (48), 41439−41449.

(5) (a) Chen, J.; Captain, B.; Takenaka, N. Helical Chiral 2,2′-Bipyridine *N*- Monoxides as Catalysts in the Enantioselective Propargylation of Aldehydes with Allenyltrichlorosilane. *Org. Lett.* **2011**, *13* (7), 1654−1657. (b) Peng, Z.; Takenaka, N. Applications of Helical-Chiral Pyridines as Organocatalysts in Asymmetric Synthesis. *Chem. Rec.* **2013**, *13* (1), 28−42.

(6) (a) Anger, E.; Iida, H.; Yamaguchi, T.; Hayashi, K.; Kumano, D.; Crassous, J.; Vanthuyne, N.; Roussel, C.; Yashima, E. Synthesis and Chiral Recognition Ability of Helical Polyacetylenes Bearing Helicene Pendants. *Polym. Chem.* **2014**, *5* (17), 4909−4914. (b) Zhang, G.; Zhang, J.; Tao, Y.; Gan, F.; Lin, G.; Liang, J.; Shen, C.; Zhang, Y.; Qiu, H. Facile Fabrication of Recyclable Robust Noncovalent Porous Crystals from Low-Symmetry Helicene Derivative. *Nat. Commun.* **2024**, *15* (1), No. 5469.

(7) Schnitzlein, M.; Shoyama, K.; Würthner, F. A Highly Fluorescent Bora[6]helicene Exhibiting Circularly Polarized Light Emission. *Chem. Sci.* **2024**, *15* (8), 2984−2989.

(8) (a) Greenfield, J. L.; Wade, J.; Brandt, J. R.; Shi, X.; Penfold, T. J.; Fuchter, M. J. Pathways to Increase the Dissymmetry in the Interaction of Chiral Light and Chiral Molecules. *Chem. Sci.* **2021**, *12* (25), 8589−8602. (b) Wang, Z.; Zeng, X.; Zhao, W.; Miao, Y.; Lu, H.; Wang, H.; Shao, T.; Niu, X.; Gull, S.; Qiao, T.; Sun, B.; Liu, X.; Zhang, H.-L.; Chen, Y.; Long, G. The Interplay between Luminescence Dissymmetry Factor and Quantum Yield: Symmetric and Asymmetric Hydrogen Bonding. *J. Am. Chem. Soc.* **2025**, *147* (41), 37771−37778.

(9) (a) Yavari, K.; Delaunay, W.; De Rycke, N.; Reynaldo, T.; Aillard, P.; Srebro-Hooper, M.; Chang, V. Y.; Muller, G.; Tondelier, D.; Geffroy, B.; Voituriez, A.; Marinetti, A.; Hissler, M.; Crassous, J. Phosphahelicenes: From Chiroptical and Photophysical Properties to OLED Applications. *Chem. - Eur. J.* **2019**, *25* (20), 5303−5310. (b) Dhbaibi, K.; Favereau, L.; Crassous, J. Enantioenriched Helicenes and Helicenoids Containing Main-Group Elements (B, Si, N, P). *Chem. Rev.* **2019**, *119* (14), 8846−8953. (c) Baciu, B. C.; Bronk, P. J.; de Ara, T.; Rodriguez, R.; Morgante, P.; Vanthuyne, N.; Sabater, C.; Untiedt, C.; Autschbach, J.; Crassous, J.; Guijarro, A. Dithia[9]-helicenes: Molecular Design, Surface Imaging, and Circularly Polarized Luminescence with Enhanced Dissymmetry Factors. *J. Mater. Chem. C* **2022**, *10* (38), 14306−14318. (d) Nowak-Król, A.; Geppert, P. T.; Naveen, K. R. Boron-Containing Helicenes as New Generation of Chiral Materials: Opportunities and Challenges of Leaving the Flatland. *Chem. Sci.* **2024**, *15* (20), 7408−7440.

(10) (a) Guy, L.; Mosser, M.; Pitrat, D.; Mulatier, J.-C.; Kukułka, M.; Srebro-Hooper, M.; Jeanneau, E.; Bensalah-Ledoux, A.; Baguenard, B.; Guy, S. Acid/Base-Triggered Photophysical and Chiroptical Switching in a Series of Helicenoid Compounds. *Molecules* **2023**, *28* (21), No. 7322. (b) Wei, R.; Tang, J.; Liu, Y.; Su, H.; Wang, H.; Ma, Z.; Shen, Z. Circularly Polarized Luminescence Signal Inversion in Aza-[7]Helicene Derivatives: Theoretical Insight into Pyridine Nitrogen Position and Protonation Effects. *ChemPhysChem* **2025**, *26* (14), No. e202500106.

(11) (a) Taipale, E.; Durandin, N. A.; Salunke, J. K.; Candeias, N. R.; Ruoko, T.-P.; Ward, J. S.; Priimagi, A.; Rissanen, K. Protonation-

https://doi.org/10.1021/jacsau.6c00315
JACS Au XXXX, XXX, XXX−XXX

Induced Fluorescence Modulation of Carbazole-Based Emitters. *Mater. Adv.* **2022**, *3* (3), 1703−1712. (b) Gounder, R. P.; Martir, D. R.; Zysman-Colman, E. Pyridine-Functionalized Carbazole Donor and Benzophenone Acceptor Design for Thermally Activated Delayed Fluorescence Emitters in Blue Organic Light-Emitting Diodes. *J. Photonics Energy* **2018**, *8* (3), No. 032106.

(12) (a) Pounder, A.; Pavlovic, M.; Chow, D.; Regan, K. T.; Chen, A.; Wetmore, S. D.; Manderville, R. A. Photobasicity-Triggered Twisted Intramolecular Charge Transfer of Push−Pull Chromophores. *J. Phys. Chem. B* **2025**, *129* (33), 8485−8493. (b) Zhu, H.; Wang, X.; Ma, R.; Kuang, Z.; Guo, Q.; Xia, A. Intramolecular Charge Transfer and Solvation of Photoactive Molecules with Conjugated Push−Pull Structures. *ChemPhysChem* **2016**, *17* (20), 3245−3251.

(13) (a) Weiß, A.; Podlech, J. Synthesis of 5,9-Diaza[5]helicenes. *Eur. J. Org. Chem.* **2019**, *2019* (39), 6697−6701. (b) Herzog, S.; Marten, I.; Weiß, A.; Podlech, J. Synthesis of Diaza[5]helicenes by *ortho*,*ortho*'-Fusion of *ortho*-Terphenyls. *Synthesis* **2022**, *54* (19), 4220−4234. (c) Herzog, S.; Rizzo, G. G.; Podlech, J. Synthesis of 5,9-Diaza Analogues of [5]- and [6]Helicene and their Chiroptic and Photophysical Characterization. *Eur. J. Org. Chem.* **2024**, *27* (14), No. e202301240. (d) Marten, I.; Podlech, J. Synthesis of Helical Indolophenanthridines Showing Aggregation-Induced Emission. *Org. Lett.* **2024**, *26* (6), 1148−1153. (e) Marten, I.; Dilanas, M. E. A.; Podlech, J. Fluorescent Carbazole-Derived Aza[5]helicenes: Synthesis, Functionalisation, and Characterisation. *Chem. - Eur. J.* **2025**, *31* (27), No. e202501081.

(14) Vallejos González, V.; Kahle, J.; Hüßler, C.; Heckershoff, R.; Hashmi, A. S. K.; Birenheide, B.; Hauser, A.; Podlech, J. Synthesis of Thiophene-Fused Helicenes. *Eur. J. Org. Chem.* **2023**, *26* (33), No. e202300545.

(15) Herzog, S.; Hinz, A.; Breher, F.; Podlech, J. Cyclopenta-Fused Polyaromatic Hydrocarbons: Synthesis and Characterisation of a Stable, Carbon-Centred Helical Radical. *Org. Biomol. Chem.* **2022**, *20* (14), 2873−2880.

(16) (a) Bucherer, H. T. Über die Einwirkung schwefligsaurer Salze auf aromatische Amido- und Hydroxylverbindungen. *J. Prakt. Chem.* **1904**, *69* (1), 49−91. (b) Damrath, M.; Caspers, L. D.; Duvinage, D.; Nachtsheim, B. J. One-Pot Synthesis of Heteroatom-Bridged Cyclic Diaryliodonium Salts. *Org. Lett.* **2022**, *24* (13), 2562−2566.

(17) Bräse, S.; Gil, C.; Knepper, K.; Zimmermann, V. Organic Azides: An Exploding Diversity of a Unique Class of Compounds. *Angew. Chem., Int. Ed.* **2005**, *44* (33), 5188−5240.

(18) Yoshikai, N.; Wei, Y. Synthesis of Pyrroles, Indoles, and Carbazoles through Transition-Metal-Catalyzed C−H Functionalization. *Asian J. Chem.* **2013**, *2* (6), 466−478.

(19) Ullah, E.; McNulty, J.; Robertson, A. Highly Chemoselective Mono-Suzuki Arylation Reactions on All Three Dichlorobenzene Isomers and Applications Development. *Eur. J. Org. Chem.* **2012**, *2012* (11), 2127−2131.

(20) Morgan, G. T.; Walls, L. P. Researches in the Phenanthridine Series. Part I. A New Synthesis of Phenanthridine Homologues and Derivatives. *J. Chem. Soc.* **1931**, 2447−2456.

(21) Zander, M.; Franke, W. H. Über Carbazolo-carbazole. *Chem. Ber.* **1969**, *102* (8), 2728−2738.

(22) Liu, P.-C.; Lei, J.; Liu, C.-C.; Fan, Y.-T.; Wu, T.-L. Rational Molecular Design for Boosting Afterglow Efficiency in Nonplanar Carbazolocarbazoles. *JACS Au* **2025**, *5* (2), 756−765.

(23) (a) Perdew, J. P.; Burke, K.; Ernzerhof, M. Generalized Gradient Approximation Made Simple. *Phys. Rev. Lett.* **1996**, *77* (18), 3865−3868. (b) Perdew, J. P.; Burke, K.; Ernzerhof, M. Generalized Gradient Approximation Made Simple (Erratum). *Phys. Rev. Lett.* **1997**, *78* (7), No. 3865. (c) Adamo, C.; Barone, V. Toward Reliable Density Functional Methods without Adjustable Parameters: The PBE0 Model. *J. Chem. Phys.* **1999**, *110* (13), 6158−6170.

(24) (a) Weigend, F.; Ahlrichs, R. Balanced Basis Sets of Split Valence, Triple Zeta Valence and Quadruple Zeta Valence Quality for H to Rn: Design and Assessment of Accuracy. *Phys. Chem. Chem. Phys.* **2005**, *7* (18), 3297−3305. (b) Weigend, F. Accurate Coulomb-Fitting Basis Sets for H to Rn. *Phys. Chem. Chem. Phys.* **2006**, *8* (9), 1057−1065.

(25) Grimme, S.; Antony, J.; Ehrlich, S.; Krieg, H. A Consistent and Accurate *ab initio* Parametrization of Density Functional Dispersion Correction (DFT-D) for the 94 Elements H-Pu. *J. Chem. Phys.* **2010**, *132* (15), No. 154104.

(26) Grimme, S.; Ehrlich, S.; Goerigk, L. Effect of the Damping Function in Dispersion Corrected Density Functional Theory. *J. Comput. Chem.* **2011**, *32* (7), 1456−1465.

(27) Ho, J.; Coote, M. L. A Universal Approach for Continuum Solvent pK_a Calculations: Are We there yet? *Theor. Chem. Acc.* **2010**, *125* (1), 3−21.

(28) Keene, B. R. T.; Tissington, P. Studies in the Phenanthridine Series. Part II. *J. Chem. Soc.* **1965**, No. 0, 4426−4429.

(29) (a) Tervola, E.; Truong, K.-N.; Ward, J. S.; Priimagi, A.; Rissanen, K. Fluorescence Enhancement of Quinolines by Protonation. *RSC Adv.* **2020**, *10* (49), 29385−29393. (b) More, Y. W.; Padghan, S. D.; Bhosale, R. S.; Pawar, R. P.; Puyad, A. L.; Bhosale, S. V.; Bhosale, S. V. Proton Triggered Colorimetric and Fluorescence Response of a Novel Quinoxaline Compromising a Donor-Acceptor System. *Sensors* **2018**, *18* (10), No. 3433.

(30) Joshi, N. K.; Joshi, H. C.; Gahlaut, R.; Tewari, N.; Rautela, R.; Pant, S. Steady State and Time-Resolved Fluorescence Study of Isoquinoline: Reinvestigation of Excited State Proton Transfer. *J. Phys. Chem. A* **2012**, *116* (27), 7272−7278.

(31) (a) Dhiman, S.; Singla, N.; Ahmad, M.; Singh, P.; Kumar, S. Protonation- and Electrostatic-Interaction-Based Fluorescence Probes for the Selective Detection of Picric Acid (2,4,6-Trinitrophenol) − an Explosive Material. *Mater. Adv.* **2021**, *2* (20), 6466−6498. (b) Jiang, G.; Ma, Y.; Ding, J.; Liu, J.; Liu, R.; Zhou, P. N-Protonation as a Switch of the Twisted Excited States with $\pi\pi^*$ or $n\pi^*$ Character and Correlation with the π-Electrons Characteristic of Rotatable Bonds. *Chem. - Eur. J.* **2023**, *29* (38), No. e202300625.

(32) Arrico, L.; Di Bari, L.; Zinna, F. Quantifying the Overall Efficiency of Circularly Polarized Emitters. *Chem. - Eur. J.* **2021**, *27* (9), 2920−2934.

(33) (a) Gong, X.; Li, C.; Cai, Z.; Wan, X.; Qian, H.; Yang, G. Synthesis of Nitrogen-Doped Aza-Helicenes with Chiral Optical Properties. *J. Org. Chem.* **2022**, *87* (13), 8406−8412. (b) Takaishi, K.; Yasui, M.; Ema, T. Binaphthyl−Bipyridyl Cyclic Dyads as a Chiroptical Switch. *J. Am. Chem. Soc.* **2018**, *140* (16), 5334−5338. (c) Tong, S.; Li, J.-T.; Liang, D.-D.; Zhang, Y.-E.; Feng, Q.-Y.; Zhang, X.; Zhu, J.; Wang, M.-X. Catalytic Enantioselective Synthesis and Switchable Chiroptical Property of Inherently Chiral Macrocycles. *J. Am. Chem. Soc.* **2020**, *142* (34), 14432−14436. (d) Yen-Pon, E.; Buttard, F.; Frédéric, L.; Thuéry, P.; Taran, F.; Pieters, G.; Champagne, P. A.; Audisio, D. Heterohelicenes through 1,3-Dipolar Cycloaddition of Sydnones with Arynes: Synthesis, Origins of Selectivity, and Application to pH-Triggered Chiroptical Switch with CPL Sign Reversal. *JACS Au* **2021**, *1* (6), 807−818.

(34) Mori, T. Circularly Polarized Luminescence of Isolated Small Organic Molecules. In *Springer eBook Collection*; Springer: Singapore, 2020.

https://doi.org/10.1021/jacsau.6c00315
JACS Au XXXX, XXX, XXX−XXX